

Clustered star formation and outflows in AFGL 2591

A. Sanna¹, M. J. Reid², C. Carrasco-González¹, K. M. Menten¹, A. Brunthaler¹, L. Moscadelli³,
K.L.J. Rygl⁴

asanna@mpifr-bonn.mpg.de

ABSTRACT

We report on a detailed study of the water maser kinematics and radio continuum emission toward the most massive and young object in the star-forming region AFGL 2591. Our analysis shows at least two spatial scales of multiple star formation, one projected across 0.1 pc on the sky and another one at about 2000 AU from a ZAMS star of about 38 M_{\odot} . This young stellar object drives a powerful jet- and wind-driven outflow system with the water masers associated to the outflow walls, previously detected as a limb-brightened cavity in the NIR band. At about 1300 AU to the north of this object a younger protostar drives two bow shocks, outlined by arc-like water maser emission, at 200 AU either side of the source. We have traced the velocity profile of the gas that expands along these arc-like maser structures and compared it with the jet-driven outflow model. This analysis suggests that the ambient medium around the northern protostar is swept up by a jet-driven shock ($> 66 \text{ km s}^{-1}$) and perhaps a lower-velocity ($\sim 10 \text{ km s}^{-1}$) wind with an opening angle of about 20° from the jet axis.

Subject headings: stars: formation — stars: individual: AFGL 2591 — ISM: kinematics and dynamics — masers — techniques: high angular resolution

1. Introduction

The study of high-mass ($> 8 M_{\odot}$) star formation still faces fundamental questions such as (e.g., Zinnecker & Yorke 2007; Beuther et al. 2007) what is the origin of the mass reservoir for the protostar (whether the protostar can gather mass only from its own cocoon or competes with the nearby protostellar companions to accrete mass from the whole molecular clump) and what is the accretion mechanism (whether the mass is conveyed to the protostar through a stable accreting disk or via episodic accreting flows while the protostar crosses the denser portions of the molecular

¹Max-Planck-Institut für Radioastronomie, Auf dem Hügel 69, 53121 Bonn, Germany

²Harvard-Smithsonian Center for Astrophysics, 60 Garden Street, Cambridge, MA 02138, USA

³INAF, Osservatorio Astrofisico di Arcetri, Largo E. Fermi 5, 50125 Firenze, Italy

⁴IFSI-INAF, Istituto di Fisica dello Spazio Interplanetario, Via del Fosso del Cavaliere 100, 00133 Roma, Italy

clump). To examine these questions, observations on linear scales matching the sizes of the molecular clumps (0.1–1 pc) need to be combined with a closer view of the protostellar surroundings (the hot molecular cores, HMCs, with sizes of a few thousands of AU) to establish the presence of multiple sources, their kinematical structures, and a possible overall interaction.

Focusing on a single protostellar core, Very Long Baseline Interferometry (VLBI) proper motion studies of maser spots in conjunction with sub-arcsecond imaging of the free-free emission of very young H II regions and thermal jets have proven a powerful tool to investigate the kinematics and the structure of the gas close to the protostar(s). For instance, our VLBI multi-epoch observations toward the massive young stellar object (YSO) G23.01-0.41 have shown three different kinematical structures traced by the H₂O, OH, and CH₃OH masing molecules within 2000 AU from the central YSO. While the water masers trace a bipolar flow associated with a thermal jet, the hydroxyl masers belong to an expanding layer in front of the central source. Furthermore, the methanol masers appear to undergo both rotation and expansion inside a toroidal structure traced in NH₃ lines and extended over about 0.1 pc (Sanna et al. 2010b).

The present paper focuses on the water masers and radio continuum toward the high-mass star-forming region AFGL 2591. The distance to this region has been substantially underestimated in the past and we have recently measured an accurate value of 3.3 kpc with the trigonometric parallax of its 22.2 GHz H₂O masers (Rygl et al. 2011, submitted). Based on the data of Minh & Yang (2008) and Lada et al. (1984), we find a revised value for the large-scale (< 10 pc) clump mass of about $2 \times 10^4 M_{\odot}$ and a bolometric luminosity inferred from IR data of $2 \times 10^5 L_{\odot}$. From observations of the ¹³CO rovibrational lines, the systemic velocity of the region (V_{sys}) with respect to the local standard of rest (LSR) is -5.7 km s^{-1} (van der Tak et al. 1999).

AFGL 2591 shows energetic star formation activity with hot core emission detected in several molecular lines (e.g., van der Tak et al. 1999; Doty et al. 2002; Benz et al. 2007; van der Wiel et al. 2011). A number of compact radio continuum sources were resolved in the region (Campbell 1984; Trinidad et al. 2003; van der Tak & Menten 2005) and associated with distinct clusters of water masers (Tofani et al. 1995; Trinidad et al. 2003), which establishes the occurrence of multiple star formation. AFGL 2591 exhibits a powerful CO outflow, which is extended more than $5' \times 5'$ ($\sim 5 \text{ pc} \times 5 \text{ pc}$), with the blue lobe toward the west and the red lobe to the northeast (e.g., Lada et al. 1984; Hasegawa & Mitchell 1995). This outflow activity is also associated with several Herbig-Haro objects toward the west (Poetzel et al. 1992) and H₂ bow shocks (Tamura & Yamashita 1992), marking the interaction between outflowing material and the surrounding molecular envelope. There is evidence for an outflow cavity that enhances the chemistry along the outflow walls far from the dust peak (e.g., Bruderer et al. 2009). This outflow cavity is observed as NIR loops, associated with the blueshifted outflow lobe, at the high resolution of 170 mas by Preibisch et al. (2003, cf. also Tamura et al. 1991; Minchin et al. 1991). The apex of these NIR loops is centered on the most compact radio continuum source in the region called VLA-3 (after Trinidad et al. 2003).

The observations reported here focus on the water maser emission within $2''$ from VLA-3. In

Sect. 2, we describe our Very Long Baseline Array (VLBA) observations of the 22.2 GHz H_2O masers together with the archival Very Large Array (VLA) A-configuration observations of the radio continuum emission at 1.3 and 0.7 cm. In Sect. 3, we illustrate the spatial morphology and kinematics of the maser emission and present results from archival VLA observations, constraining the properties of the radio continuum associated with the masers. Section 4 discusses the properties of each cluster of water maser emission detected in the region and draws an overall view for the purposes of star formation. The main conclusions are summarized in Sect. 5.

2. Observations and Data Analysis

2.1. VLBA observations: 22.2 GHz H_2O masers

We conducted VLBA¹ observations in the K band to study the $6_{16} - 5_{23}$ H_2O maser emission (rest frequency 22.235079 GHz) toward AFGL 2591. The VLBA observations were scheduled under program BM272H at four epochs: 2008 November 10, 2009 May 6, 13, and November 13. While these observations were optimized to measure the annual parallax and Galactic proper motion of the source (Rygl et al. 2011, submitted), in this paper we focus on the internal kinematics of the water maser emission.

We performed phase-referencing observations by fast switching between the maser target and the ICRF calibrator J2007+4029. That allowed us to determine the water masers absolute position within an accuracy of ± 1 mas. Two fringe finders (3C345 and 3C454.3) were observed for bandpass, single-band delay, and instrumental phase-offset calibration. Further details about these observations as well as the distance measurement to AFGL 2591 can be found in Rygl et al. (2011, submitted). We employed four adjacent IFs of 8 MHz bandwidth in dual circular polarization, each one split into 256 spectral channels. This receiver setup provided both a large-enough bandwidth to increase the SNR of the weak continuum calibrators and a 0.42 km s^{-1} channel width to adequately sample the maser lines. The third IF centered on an LSR velocity (V_{LSR}) of -5.0 km s^{-1} covered the previous detections of water maser emission in the region (Trinidad et al. 2003). The data were processed with the VLBA correlation facility in Socorro (New Mexico) using an averaging time of about 0.9 s which limited the instantaneous field of view of the interferometer to about $2''$ (i.e. without significant amplitude losses). Data were reduced with the NRAO Astronomical Image Processing System (AIPS) following the procedure described in Reid et al. (2009a).

The natural CLEAN beam was an elliptical Gaussian with an FWHM size of $0.80 \text{ mas} \times 0.40 \text{ mas}$ at a P.A. of -14.9° (east of north), with small variations from epoch to epoch. In each observing epoch, with an on-source integration time of about 2 h, the effective rms noise level on the channel maps was about $0.01 \text{ Jy beam}^{-1}$. The total-power spectrum of the 22.2 GHz masers

¹The VLBA is operated by the National Radio Astronomy Observatory (NRAO). The NRAO is a facility of the National Science Foundation operated under cooperative agreement by Associated Universities, Inc.

toward AFGL 2591 is shown in Figure 1.

2.2. VLA archival data

We retrieved VLA A-configuration observations toward AFGL 2591 at 1.3 and 0.7 cm from the VLA² archive for the purposes of a detailed comparison with the high-resolution VLBA maser data. These observations were scheduled on 1999 June 29 (Trinidad et al. 2003) and 2002 March 23 (van der Tak & Menten 2005), respectively. We recalibrated these data with the NRAO AIPS software package using standard procedures and cross-calibration between the strong H₂O maser lines and the continuum at 1.3 cm (e.g., Reid & Menten 1990). For the 1.3 cm data, we cleaned the VLA maps with a circular restoring beam, equal to the natural-beam minor axis for a “ROBUST 0” weighting (Table 1).

3. Results

3.1. 22.2 GHz H₂O masers

We imaged a range of LSR velocities between -40 to +25 km s⁻¹ with a field-of-view of 1''.4 × 1''.4 about the VLA-3 radio source. These limits include the emission previously reported by Trinidad et al. (2003, their Table 3 and 4) toward VLA-3. In the following, the term *feature* refers to spots spatially overlapping in contiguous velocity channels, that we treat as an individual masing cloud (see Sanna et al. 2010a for a detailed discussion).

We identified 80 distinct water maser features distributed within an area of about 0''.77 × 0''.48 (~ 2500 AU × 1500 AU). They are mainly grouped in five clusters labeled in Table 2 north-west (NW), middle-west (MW), north-east (NE), middle-east (ME), and south-east (SE) in Figure 2a. The properties of individual features are presented in Table 2 and show peak brightness ranging from 22 Jy beam⁻¹ to a detection limit of 0.05 Jy beam⁻¹ (5σ). Water maser features redshifted with respect to the V_{sys} (of -5.7 km s⁻¹) belong to the MW cluster, whereas the blueshifted emission is clustered toward the SE. The full spread in LSR velocities ranges from -0.4 km s⁻¹ for the most redshifted feature (# 13) to -34 km s⁻¹ for the most blueshifted one (# 77). The angular distribution and full-space motions of the water masers (i.e. line-of-sight velocities plus proper motions) are plotted in Figure 2a. With a time baseline of 1 yr, we measured relative proper motions of individual features with an uncertainty less than 3 km s⁻¹. Positions and velocities in Table 2 are relative to the compact feature # 4 which was stable in the spectral domain over the 1 yr observations. The magnitude of relative proper motions ranges from 5.0 km s⁻¹ for feature # 17 to 56 km s⁻¹ for feature # 54. Relying on the symmetry of the maser spatial distribution, we

²The VLA is operated by the NRAO.

have corrected the proper motions by the average velocity of all features of $V_x = 8.8 \pm 0.4$ and $V_y = 9.0 \pm 0.4$, to approximate the actual motions with respect to the center of expansion.

In Figure 2b, 2c, and 2f, we zoom in on the three water maser clusters labeled MW, NE, and SE, showing a symmetric expansion away from their centroids. The NE and SE clusters are particularly interesting due to their full kinematics and are discussed in detail in Section 4.1 and 4.2, respectively.

In Figure 2d–e, we overlay the radio continuum emission described in Section 3.2 with the water maser emission from the second epoch observations. This maser emission was summed over the full velocity range of the SE cluster (from V_{LSR} of -34 to -14 km s $^{-1}$). Its projected shape along the plane of the sky delineates a straight “V” (hereafter the H $_2$ O V-shape) with a full opening angle of $110^\circ \pm 10^\circ$ and a P.A. of 256° . The variation of LSR velocities along this V-shape is quite regular, ranging from a maximum of -13 km s $^{-1}$ (feature # 78) at the northern side of the V-shape to a minimum of about -33 km s $^{-1}$ (feature # 77) toward the southern side.

3.2. Radio continuum emission

Our measurements of the 1.3 and 0.7 cm continuum emissions are summarized in Table 1 and plotted in Figure 2d–e. Published VLA C-configuration observations at 0.7 cm show that significant emission is resolved out with the VLA A-configuration, missing more than half of the flux measured in the compact configuration (van der Tak & Menten 2005). The relative position of the 1.3 cm continuum with respect to the reference maser feature in Table 2 is obtained by matching the overall water maser distribution between the VLBA and VLA–A maps. We note that the NS spread of the maser emission overlaid on the radio continuum (~ 50 mas) have remained almost stationary over about ten years (cf. Trinidad et al. 2003).

The peak position of the 0.7 cm continuum is assumed to be aligned with the 1.3 cm peak. The three-lobed geometry of the 7 mm emission follows the 1.3 cm elongation toward the east and it branches off toward the west matching the H $_2$ O V-shape (Table 1). While this matching is particularly striking, we note that more sensitive, Q-band, observations are mandatory to confirm the spatial structure of the 0.7 cm emission. Because of the stability of the water maser distribution, but also the similarities between the morphology of the water maser emission and the 0.7 cm continuum (Figure 2e), we estimate a relative position accuracy between the radio continuum and water masers of $\pm 0''.01$.

Previous observations spanning a broad-band spectrum between 6 cm to 1.3 mm show that the spectral index ($S \propto \nu^\gamma$) for wavelengths longer than 7 mm is dominated by free-free emission ($\gamma \sim 0.9$), whereas at shorter wavelengths the flux density is mostly due to dust emission ($\gamma > 2$; van der Tak & Menten 2005 and reference therein).

4. Discussion

4.1. Outflow emission in the NE H₂O cluster

In this section, we discuss two basic characteristics observed in the NE water maser cluster (Figure 2b). Firstly, we detected two arc-like filaments of water maser emission elongated in the NE–SW direction with no emission in between them. Secondly, these arc-like filaments expand from each other with proper motions increasingly aligned with the NE–SW direction as one approaches this direction. Bipolar distributions of water masers with expanding proper motions have been reported in a large number of star-forming regions (e.g., Gwinn et al. 1992; Sanna et al. 2010b; Moscadelli et al. 2011). These detections were interpreted as footprints of the interaction between collimated jets and/or wide-angle winds from YSOs with the surrounding molecular envelope. Following this evidence, we want to show that the overall kinematics of the NE water maser cluster can be explained by assuming that a single object, in between the maser emission, emits a high-velocity, bipolar jet along the NE–SW direction (Figure 2b and 3a). At first, we will compare the velocity profile of the water masers along the arc-like structures with the model of jet-driven outflows presented in Ostriker et al. (2001) and Lee et al. (2001). The jet model predicts that the interaction between a bow shock and the ambient material gives an upper and lower limit to the velocity of the processed material. This processed material is a mixture of material that was already part of the bow shock and material incorporated from the ambient medium as the shock front expands. The shock front delineates an arc-like structure (as do the masers) and the velocity component along the jet axis decreases roughly as $r^{-2/3}$, where r is the offset distance from the head of the jet (e.g., Figure 2 in Ostriker et al. 2001).

The similarities of the spatial elongation and velocities of the water masers would be naturally explained if the NE–SW direction is associated with an outflow in this direction. In Figure 3a, we define an elliptical symmetry that matches to first order both the width and the NE–SW elongation of the water maser distribution with a simple central symmetry (major axis and eccentricity on top of Figure 3a). This elliptical pattern allows us to define a new reference frame with origin at the center of the ellipse ($\Delta x = 625$ mas and $\Delta y = 260$ mas w.r.t. the reference feature in Table 2) and x , y axes along the minor (R) and major (z) axes of the ellipse, respectively. This reference frame is tilted by 22° to the east of the north direction. Due to the small dispersion of LSR velocities (1.5 km s^{-1}) centered at about -7.9 km s^{-1} , we also assume that all the maser features lie along the same plane. We want to study the velocity profile of the shock fronts traced by the water maser proper motions with respect to the new z – R reference frame. In the following, we use the same terminology of Ostriker et al. (2001) and Lee et al. (2001) in order to facilitate the comparison with their jet model.

In Figure 3b, we report the behavior of the velocity components (V_z) of the water masers along the major axis of the ellipse (z). The idea that the z -direction is a preferred outflow direction is supported by the velocity profile in Figure 3b, which resembles that expected for a ballistic bow-shock produced by a jet along the z -direction (cf. Figure 4 of Lee et al. 2001). For such a

bow-shock model velocities are constrained in Figure 3b by two solid lines and the expected gas velocity should lie between them. These limits are derived from equations (22), (18), and (20) of Ostriker et al. (2001) and define the bow shock profile $z = f(R)$, the mean velocity of the mixing of jet and ambient material v'_z (solid line) in a shell, and the velocity of newly shocked ambient material u'_z (dashed steeper line), respectively. These equations are parameterized by the jet radius R_j , the velocity of the bow shock v_s , and the ejection velocity βc_s of the material processed by the working surface, expressed as a multiple of the isothermal sound speed (Ostriker et al. 2001). For the radius of the high-velocity “core” of the jet (R_j), we set the minimum projected distance to the R-axis measured with the masers of 1.8 mas (≈ 6 AU). This value implies a width-to-length ratio of the jet from the center of the ellipse of 0.05, consistent with that found in the literature for H_2 jets at typical scales of $10^3 - 10^4$ AU (e.g., HH 212 in Zinnecker et al. 1998). We stress that R_j is the only constraint we put on the model, whereas we consider the best value of the ratio $\beta c_s/v_s = 0.5$ and $\beta = 4.1$ inferred from the simulations by Lee et al. (2001). By setting the tip of the bow shock at the maximum maser projection along z (the “0” in Ostriker et al. 2001), we find a good agreement of the measured maser velocities (black squares in Figure 3b) with the jet-driven outflow model. We note that the maser velocities are closer to the ambient material velocity (dashed line) in agreement with simulations by Lee et al. (2001, their Figure 4). This behavior may reflect an incomplete mixing of material already in the bow shock shell and material added from the ambient medium. The $\beta c_s/v_s$ ratio implies a bow shock speed of about 66 km s^{-1} for a sound speed of 8 km s^{-1} at the cooling cutoff of 10^4 K (see Ostriker et al. 2001). On the contrary, in the alternative scenario of a wide-angle wind the V_z motions would increase linearly with z , that is not observed (e.g., Lee et al. 2001 their Figure 9). This suggests that the maser cloudlets are dragged along the z -direction by a jet-driven shock component.

On the other hand, the jet-driven outflow model predicts an upper limit to the transverse velocity component V_R with respect to the jet direction of the order of the sound speed ($\sim 8 \text{ km s}^{-1}$; see Figure 3 in Ostriker et al. 2001 and Figure 4 in Lee et al. 2001). This limit is intimately related to the assumption that the transverse radial forces are dominated by thermal pressure gradients that act at the head of the jet. In Figure 3c, we measure the greatest deviations from the jet model far from the head of the jet, at an inclination of about 20° from the jet axis. This behavior may suggest that, away from the head of the jet, thermal pressure gradients no longer dominate the expansion. One possibility would be that a low-velocity ($< 10 \text{ km s}^{-1}$) wind with a wide opening angle (ca. 20°) acts with the jet simultaneously. In the wind-driven outflow model, the expansion of the outflow away from the central axis is driven by the ram pressure of a wide-angle wind (Shu et al. 1991): the V_R velocity is maximum far from the tip of the outflow shell and goes to zero at its tip (Figure 9 in Lee et al. 2001). The simultaneous presence of the two types of outflow mechanisms would agree with the hypothesis that any outflow contains a wide-angle wind at some level, in order to explain typical width-to-length ratio of about 1 : 10, much higher than in a “pure jet model” (e.g., Arce et al. 2007).

Finally, if the single jet-driven model is correct, we can also get an estimate of the dynamical

age of the jet-event exciting the water masers. The velocity of the jet (v_j) is related to the bow shock speed (v_s) by the ratio of the jet-to-ambient density, where v_s approximates v_j if the jet density exceeds the ambient density (see Ostriker et al. 2001). By considering the lower limit $v_j \approx v_s$, the inferred value of $v_s = 66 \text{ km s}^{-1}$, and the value of the higher maser projection along z , we obtain a dynamical age of $t = z_{\text{maj}}/v_j \simeq 14 \text{ yr}$. On the one hand, this dynamical age is consistent with other estimates based on the expanding motions of masers around forming YSOs (e.g., Torrelles et al. 2003, Moscadelli et al. 2007). On the other hand, given how unlikely it would be to observe such a short-lived event, it strongly suggests that we are tracing a recurrent phenomenon of ejection of matter from an YSO. That would favor a pulsed-jet paradigm against a steady-jet one as supported, for instance, by the recurrent knots and bow shocks observed in the prototypical Herbig-Haro object 212 (Zinnecker et al. 1998). This interpretation naturally explains also the eastern water masers in Figure 3a (features # 38, 39 in Table 2) and the masers at about 150 mas to the south of the NE cluster (the ME cluster in Table 2). These masers would belong to an older jet emission from the same object.

4.2. Outflow emission in the SE H₂O cluster associated with VLA–3

In this section, we discuss three characteristics observed in the SE water maser cluster: I. the projected V–shape of the water maser distribution on the plane of the sky, “pointing” toward the peak of the radio continuum emission (Figure 2d–e); II. the water maser proper motions that mainly expand along the V–shape (Figure 2a); III. the line-of-sight velocity gradient observed through the V–shape, with velocities increasing to the south (Figure 2f). In the following, we relate these properties with the large-scale outflow and the nature of the radio continuum emission and suggest that the H₂O masers trace the edges of the outflow cavity associated with a massive YSO (see Figure 4a).

The H₂O emission from the SE cluster is blueshifted with respect to the overall velocity of the cloud (-5.7 km s^{-1}) and covers a range of line-of-sight velocities consistent with the small-scale, blueshifted wing of the CO(3–2) outflow (between -10 and -40 km s^{-1} ; Hasegawa & Mitchell 1995). The V–shape observed in the water maser emission opens toward the west, where a limb-brightened cavity was previously outlined as NIR loops (Tamura et al. 1991; Minchin et al. 1991; Preibisch et al. 2003). These loops were explained as wind-bubbles, which were created as the blueshifted (western) side of the outflow pushed against the environment and swept up ambient material (Preibisch et al. 2003). We note that the wide opening angle of the NIR loops ($> 100^\circ$) is consistent with that of the V–shape (110°). Actually, if the loops outlined the outflow cavity, one might expect the water masers along the outflow walls, where shocks are more likely. The H₂O V–shape opens toward a position angle (P.A.= 256°) in good agreement with the direction of the western side of the outflow, which has been detected in a number of tracers: i) the NIR bright loops, with a $262^\circ \leq \text{P.A.} \leq 256^\circ$, surrounding the outflow cavity with a symmetry axis at a P.A. of 259° (e.g., Preibisch et al. 2003, see their Figure 3); ii) the blueshifted CO lobe with a P.A. of

about 260° (e.g., Hasegawa & Mitchell 1995, see their Figure 4); iii) the western, aligned, Herbig-Haro objects with a $258^\circ \leq \text{P.A.} \leq 261^\circ$ (Poetzel et al. 1992) and the hot H_2 knots in the same direction (Tamura & Yamashita 1992); iv) the elongated 1.3 cm continuum with a P.A. of 268° and a spectral index consistent with an ionized wind (Figure 2d). If water masers would belong to the blueshifted outflow lobe, and might possibly amplify the continuum background at 1.3 cm, it would naturally explain the non-detection of redshifted maser emission, that would belong to the receding outflow lobe. Also, since the outflow axis is close to the line-of-sight (within $30^\circ - 45^\circ$; Minchin et al. 1991; Hasegawa & Mitchell 1995; van der Tak et al. 1999), this scenario agrees with the direction of the maser proper motions, that are mainly expanding parallel to the V-shape with a strong component toward the observer (Figure 4). The velocity gradient observed across the maser V-shape (Figure 2f) might be reproduced with a slow precession of the outflow axis about the mean direction Z_{out} in Figure 4 (as speculated at first by Trinidad et al. 2003).

The strong water masers and the radio continuum emission from VLA-3 (Figure 2d–e) suggest an association with a massive YSO (van der Tak & Menten 2005). If the free-free emission longward of 7 mm wavelength originates from an ionized wind, we can estimate a lower limit to the mass-loss rate (\dot{M}_w) of the wind and put a constraint to the nature of the driving source. We apply equation (4) of Rodriguez & Canto (1983) and use the flux at 1.3 cm to estimate the mass-loss rate in the assumption of a spherical, isothermal, completely photoionized, uniform wind:

$$\left(\frac{\dot{M}_w}{10^{-5} \text{ M}_\odot \text{ yr}^{-1}} \right) \approx 1.7 \left(\frac{S_\nu}{1.6 \text{ mJy}} \right)^{3/4} \left(\frac{\nu}{22.2 \text{ GHz}} \right)^{-0.45} \cdot \left(\frac{d}{3.3 \text{ kpc}} \right)^{3/2} \left(\frac{v_w}{10^3 \text{ km s}^{-1}} \right), \quad (1)$$

where v_w is the velocity of the wind. We have considered the accurate value of the recently measured distance to AFGL 2591 and a wind velocity of several 10^2 km s^{-1} , reported in both the [SII] lines by Poetzel et al. (1992) and the IR ^{12}CO broad wings by van der Tak et al. (1999). The assumption of a spherical wind is justified by the wide opening angle observed both with the maser emission and the NIR loops ($> 100^\circ$). Note that, Trinidad et al. (2003) used the lower flux at 3.6 cm to estimate the mass-loss rate, based on their model with a dusty disk that would have affected the flux at 1.3 cm. Still, at the new measured distance of 3.3 kpc, their modeled flux would decrease by a factor 10 and no longer be applicable, while the spectral index for wavelengths longer than 0.7 cm suggests an origin in a ionized wind (van der Tak & Menten 2005). The mass-loss rate from equation (1) implies a photoionizing ZAMS star of type O9, with a rate of ionizing photons (N_L) of about $1.2 \times 10^{48} \text{ s}^{-1}$ (Rodriguez & Canto 1983). We compare this value with the estimates of mass and Lyman continuum flux derived by assuming a single star dominating the IR luminosity of the region. Following van der Tak & Menten (2005), we used the theoretical HR diagram by Maeder & Meynet (1989) to estimate the mass and effective temperature of a star with an IR luminosity of $2 \times 10^5 \text{ L}_\odot$; then, we used the stellar atmosphere models by Schaerer & de Koter (1997) to convert effective temperatures to Lyman fluxes. These new values of M and N_L are about

$38 M_{\odot}$ and $2 \times 10^{49} \text{ s}^{-1}$, respectively. The estimates of Lyman flux obtained independently from the radio continuum emission and the IR luminosity of the region agree within an order of magnitude. Since the former one is a lower limit derived close to the source whereas the later one gives an upper limit to the number of Lyman photons emitted over a larger field of view, this calculation provides evidence that a single massive object dominates the IR energetics of the region (according to the high-resolution NIR image of Preibisch et al. 2003).

4.3. Clustered star formation around VLA–3

We finally collect the information from the water masers and the radio continuum emission about the ongoing star formation in the region. Taking into account a possible bias of detecting only a small number of (bright) sources, there is evidence of *at least* two clustering scales for star formation in the region. One on a linear scale of about 0.1 pc on the sky, from continuum sources VLA–1, VLA–2, and VLA–3 detected at first by Campbell (1984, named by Trinidad et al. 2003). The other scale is an order of magnitude smaller and comes from our observation of at least three centers of expansion that pinpoint two other centers of star formation (the NE and MW cluster), separated by about 2000 AU on the sky from the VLA–3 radio source. Note that, the NW maser cluster might be either associated with the MW cluster or trace a further young object. Our analysis in Section 4.2 shows that VLA–3 is the most massive ($\lesssim 38 M_{\odot}$) and young object in the field dominating the IR luminosity. Several lines of arguments from the spatial scale of the maser distribution also strengthen the association between VLA–3 and the large-scale dynamics of the molecular envelope, as traced by both jet “footprints” (HH objects and H_2 knots) and the wide-angle outflow seen at the sub-parsec scale (~ 0.5 pc from VLA–3). The other two objects indicated by water maser emission in Figure 2 (the NE and MW cluster) were not detected at cm and mm wavelengths. We give an upper limit to their flux density at 1.3 cm of about 0.5 mJy (3σ). On the one hand, by assuming this radio continuum would come from a photoionized stellar wind, we can put an upper limit on the spectral type of the exciting YSOs. Following equation (1) of Rodriguez & Canto (1983) which gives the rate of ionizing photons required to fully ionize a constant velocity wind, we get a value of $N_L \lesssim 10^{47} \text{ s}^{-1}$ that would imply a ZAMS star with a spectral type later than B0. On the other hand, the high, isotropic, maser-luminosity of the NE and MW objects ($2.5 \times 10^{-5} L_{\odot}$ and $3.3 \times 10^{-5} L_{\odot}$, respectively) would suggest they are not even low-mass YSOs but possibly late B-type stars, by comparison with the SE cluster luminosity ($1.2 \times 10^{-5} L_{\odot}$) and the H_2O luminosity usually associated with low-mass stars ($< 10^{-7} L_{\odot}$; e.g., Furuya et al. 2003 and their erratum)³. In the formulation of Reid & Moran (1988), the maser luminosity is a consequence of the dissipation in the ambient cloud of the mechanical energy of the outflow from a young star, and thus could be related to the mass of the driving source.

³Note that from Trinidad et al. (2003), the isotropic maser-luminosity associated with the VLA–2 radio source is of about $4 \times 10^{-5} L_{\odot}$ (their Table 2) whereas VLA–1 does not show water maser emission.

5. Summary and Conclusions

We have presented multi-epoch, VLBA, H₂O maser observations toward the most compact radio source (i.e. VLA–3) in the high-mass star-forming region AFGL 2591. We have also compared the maser distribution with the brightness structure of the radio continuum at 1.3 and 0.7 cm observed with the VLA. Our main conclusions can be summarized as follows:

1. We have detected three main clusters of water maser emission above a detection limit of $0.05 \text{ Jy beam}^{-1}$ (5σ) within $\sim 2000 \text{ AU}$ on the sky from the VLA–3 radio source (the SE water maser cluster). Each water maser cluster shows internal expansion with velocities of a few tens of km s^{-1} (Figure 2a). A global view of the star formation activity in AFGL 2591 shows at least two spatial scales of star formation, one projected across 0.1 pc on the sky and another one at a ten times smaller scale as indicated by water maser emission.
2. The kinematics of the NE water maser cluster shows characteristics of two symmetric, jet-driven, bow shocks expanding about 200 AU from a still undetected protostar, with a velocity of about 66 km s^{-1} (Figure 2b). Our analysis of the water maser proper motions, compared to different outflow models, suggests that the primary wind may be a combination of a jet and a lower-velocity wind tilted about 20° from the jet axis. The short dynamical age (14 yr) of these expanding motions suggests they are probably related to recurrent ejection events from the central protostar(s).
3. Our analysis of the radio continuum emission compared with the IR luminosity of the region shows that VLA–3 is likely a ZAMS star with a spectral type between O9–O6 and a mass in the range $20 - 38 \text{ M}_\odot$. This young stellar object dominates the IR luminosity of the region. The water maser emission associated with VLA–3 expands toward the observer with velocities up to 50 km s^{-1} and traces a V-shape along the plane of the sky (Figure 2d–f). The orientation of the maser V-shape is aligned with the high-velocity wings of the CO outflow and the Herbig-Haro objects at a few tenth of pc from the star. The wide opening angle of the maser V-shape ($\sim 110^\circ$) agrees with that of the outflow as inferred from NIR emission along the edges of the outflow cavity. This water maser emission is likely amplified along the walls of the blueshifted outflow lobe from VLA–3 (Figure 4).

We thank J. M. Torrelles and A. P. Lobanov for helpful discussions in preparation. This work was partially funded by the ERC Advanced Investigator Grant GLOSTAR (247078). KLJR is funded by an ASI fellowship under contract number I/005/07/1.

Facilities: VLBA.

REFERENCES

- Arce, H. G., Shepherd, D., Gueth, F., et al. 2007prpl.conf, 245
- Benz, A. O., Stäuber, P., Bourke, T. L., et al. 2007, *A&A*, 47
- Beuther, H., Churchwell, E. B., McKee, C. F., & Tan, J. C. 2007prpl.conf, 165
- Bruderer, S., Benz, A. O., Bourke, T. L., & Doty, S. D. 2009, *A&A*, 503, L13
- Campbell, B. 1984, *ApJ*, 287, 334
- Doty, S. D., van Dishoeck, E. F., van der Tak, F. F. S., & Boonman, A. M. S. 2002, *A&A*, 389, 446
- Furuya, R. S., Kitamura, Y., Wootten, A., Claussen, M. J., & Kawabe, R. 2003, *ApJS*, 144, 71
- Gwinn, C. R., Moran, J. M., & Reid, M. J. 1992, *ApJ*, 393, 149
- Hasegawa, T. I., & Mitchell, G. F. 1995, *ApJ*, 451, 225
- Lada, C. J., Thronson, H. A., Jr., Smith, H. A., Schwartz, P. R., & Glaccum, W. 1984, *ApJ*, 286, 302
- Lee, C.-F., Stone, J. M., Ostriker, E. C., & Mundy, L. G. 2001, *ApJ*, 557, 429
- Maeder, A., & Meynet, G. 1989, *A&A*, 210, 155
- Minchin, N. R., Hough, J. H., McCall, A., et al. 1991, *MNRAS*, 251, 508
- Minh, Y. C., & Yang, J. 2008, *JKAS.*, 41, 139
- Moscadelli, L., Goddi, C., Cesaroni, R., Beltrán, M. T., & Furuya, R. S. 2007, *A&A*, 472, 867
- Moscadelli, L., Cesaroni, R., Rioja, M. J., Dodson, R., & Reid, M. J. 2011, *A&A*, 526, A66
- Poetzel, R., Mundt, R., & Ray, T. P. 1992, *A&A*, 262, 229
- Preibisch, T., Balega, Y. Y., Schertl, D., & Weigelt, G. 2003, *A&A*, 412, 735
- Ostriker, E. C., Lee, C.-F., Stone, J. M., & Mundy, L. G. 2001, *ApJ*, 557, 443
- Reid, M. J., & Moran, J. M. 1988, in *Galactic and Extragalactic Radio Astronomy*, ed. G. L. Verschuur & K. I. Kellermann (New York: Springer), 255
- Reid, M. J., & Menten, K. M. 1990, *ApJ*, 360, L51
- Reid, M. J., Menten, K. M., Brunthaler, A., et al. 2009a, *ApJ*, 693, 397
- Rodriguez, L. F., & Canto, J. 1983, *RMxAA*, 8, 163

- Sanna, A., Moscadelli, L., Cesaroni, R., et al. 2010a, A&A, 517, A71
- Sanna, A., Moscadelli, L., Cesaroni, R., et al. 2010b, A&A, 517, A78
- Schaerer, D., & de Koter, A. 1997, A&A, 322, 598
- Shu, F. H., Ruden, S. P., Lada, C. J., & Lizano, S. 1991, ApJ, 370, L31
- Tofani, G., Felli, M., Taylor, G. B., & Hunter, T. R. 1995, A&AS, 112, 299
- Tamura, M., Gatley, I., Joyce, R. R., et al. 1991, ApJ, 378, 611
- Tamura, M., & Yamashita, T. 1992, ApJ, 391, 710
- Torrelles, J. M., et al. 2003, ApJ, 598, L115
- Trinidad, M. A., et al. 2003, ApJ, 589, 386
- van der Tak, F. F. S., van Dishoeck, E. F., Evans, N. J., II, Bakker, E. J., & Blake, G. A. 1999, ApJ, 522, 991
- van der Tak, F. F. S., & Menten, K. M. 2005, A&A, 437, 947
- van der Wiel, M. H. D., van der Tak, F. F. S., Spaans, M., et al. 2011, A&A, 532, A88
- Zinnecker, H., McCaughrean, M. J., & Rayner, J. T. 1998, Nature, 394, 862
- Zinnecker, H., & Yorke, H. W. 2007, ARA&A, 45, 481

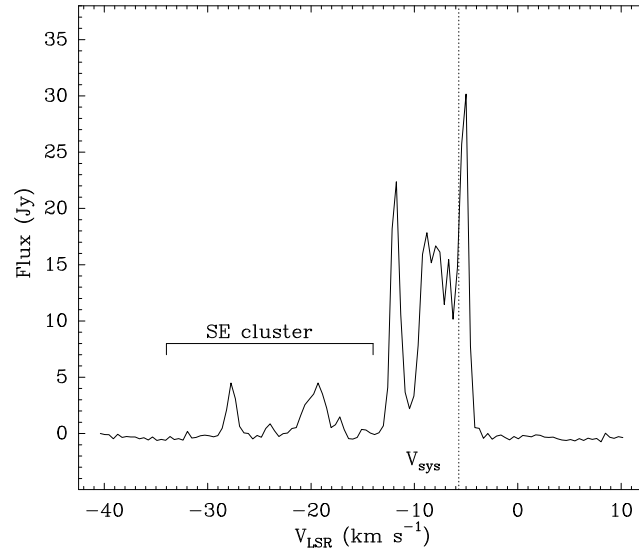


Fig. 1.— Total-power (Stokes I) spectrum of the 22 GHz H₂O masers toward AFGL 2591 from the second (middle) epoch on 2009 May 6. This profile was produced by averaging the total-power spectra of all VLBA antennas, after weighting each spectrum with the antenna system temperature. The dotted line crossing the spectrum (at -5.7 km s^{-1}) represents the systemic velocity (V_{sys}) of the molecular cloud hosting the star-forming region. The LSR velocity range from the SE water maser cluster is shown.

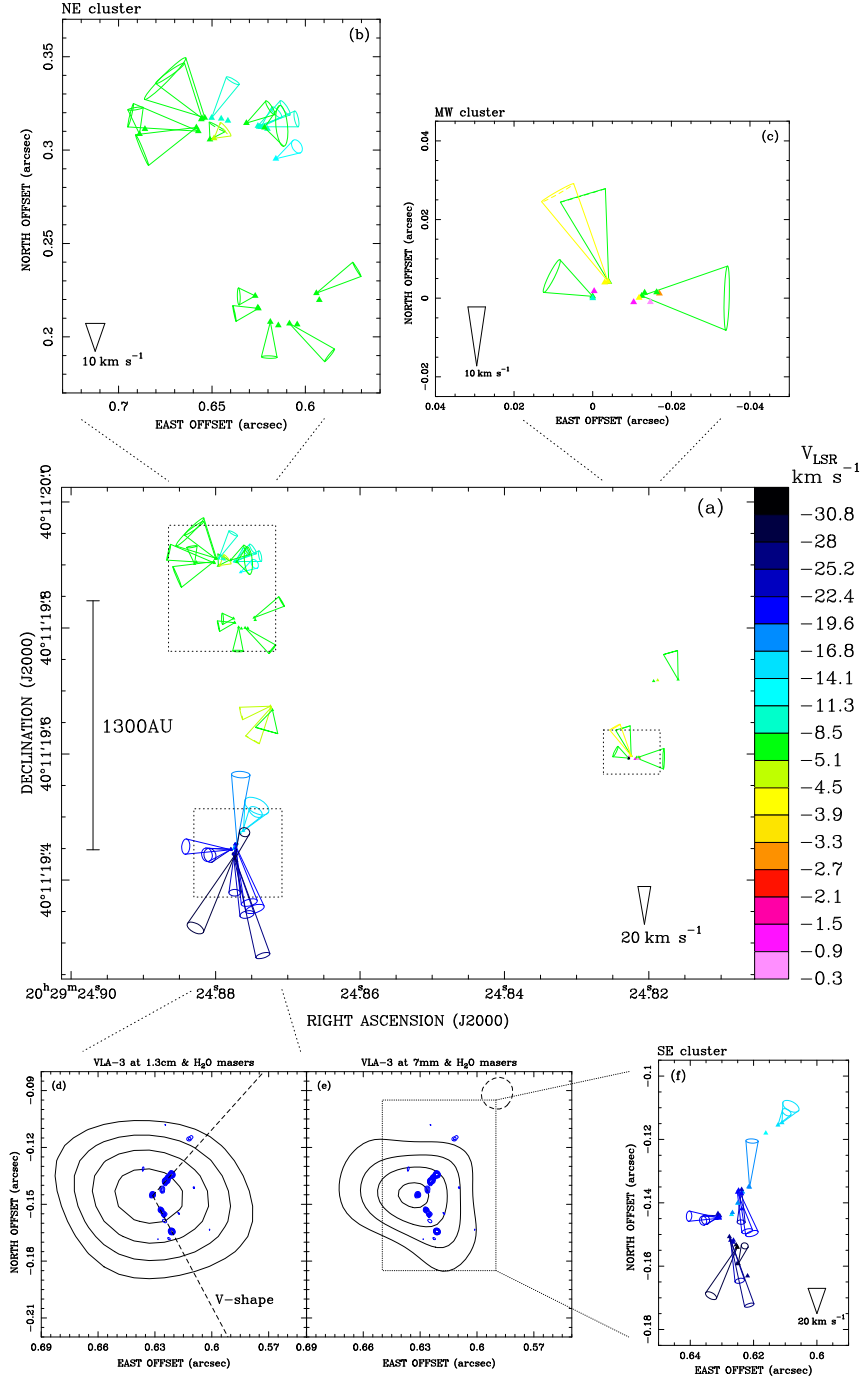


Fig. 2.— 22.2 GHz H_2O maser kinematics and radio continuum toward the VLA-3 source in AFGL 2591. *Central Panel:* Absolute positions (triangles) and internal proper motions of the 22 GHz H_2O maser features (see Table 2). Colored cones are used to show both the direction and the uncertainty (cone aperture) of the 3-D velocities of maser features. The proper-motion amplitude scale and linear-size scale are given (10 mas = 33 AU). Different colors mark the maser LSR velocities according to the righthand side scale, centered on the systematic velocity of the HMC (green equal to -5.7 km s^{-1}). *Upper Panels:* Details of the proper motions in the NE and MW water maser clusters. Relative positions refer to the phase-reference feature # 4 in Table 2. *Bottom Panels:* from left to right, detail of the extended water maser emission (blue contours) overlapped to the VLA-3 radio component of Trinidad et al. (2003), in the same reference frame of the upper panels. Blue contours are spaced by 3σ starting from a 3σ rms of $0.39 \text{ Jy beam}^{-1}$. For the VLA-A radio continuum maps (black contours), plotted levels at 1.3 cm are spaced by 1σ starting from a 3σ rms, whereas for the 7 mm map contours are -3σ , 3σ , 5σ , 7σ , and 9σ (see Table 1). A blow-up of the water maser proper motions associated with VLA-3 is shown.

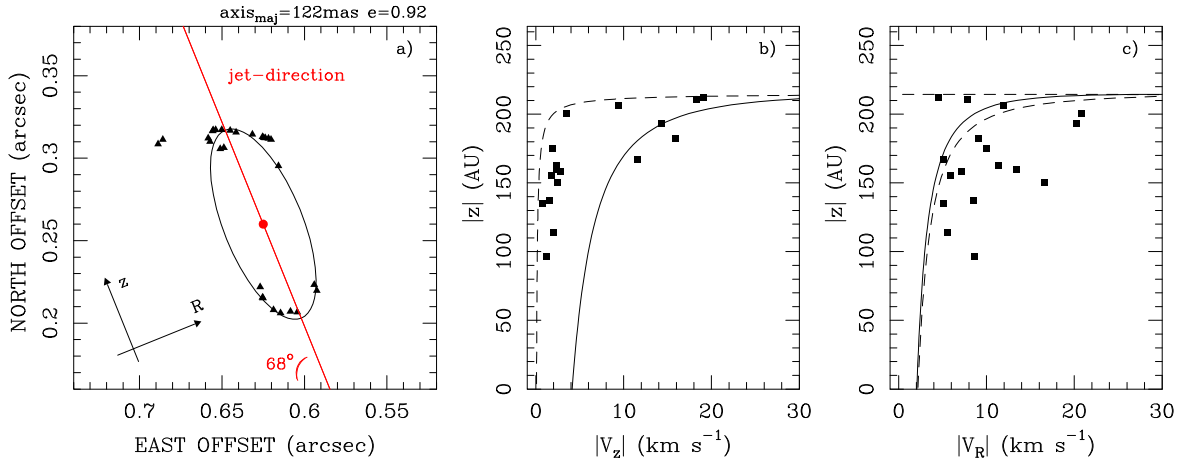


Fig. 3.— Symmetry and velocity profiles of the NE water maser cluster. *Left Panel:* Spatial distribution of water maser features (triangles) superposed to the elliptical toy model used to define the new z - R reference frame. The major axis and eccentricity of the ellipse are reported on top of the panel. *Middle Panel:* Velocity profile of the water maser proper motions along the z -direction in astronomical units. The lines represent the upper (solid line) and lower (dashed line) limits to the bow shock model of Ostriker et al. (2001) discussed in Section 4.1. *Right Panel:* Velocity profile of the transverse component, with respect to the z -direction, of the water maser proper motions as a function of z . The lines have the same meaning as in the Middle Panel.

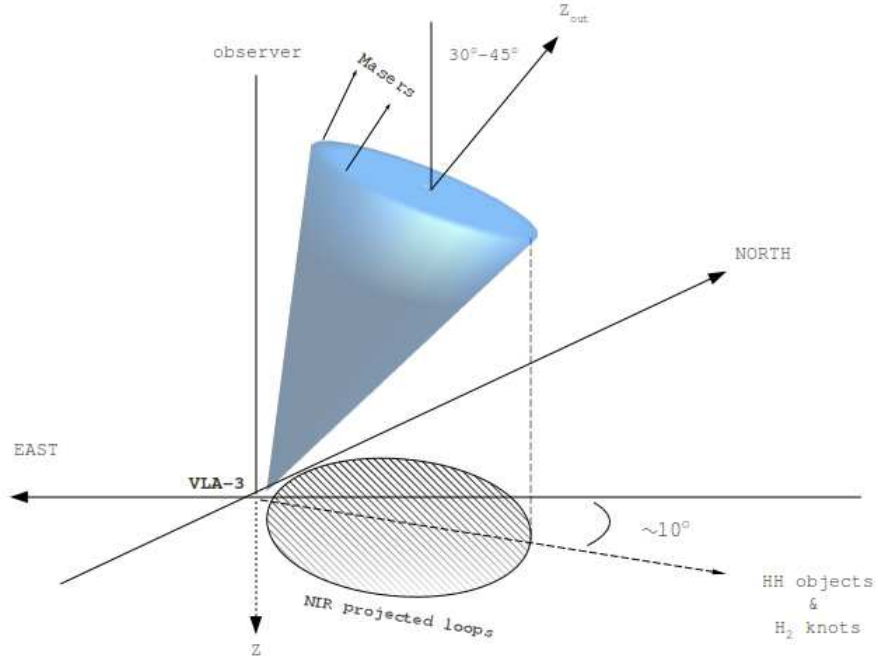


Fig. 4.— Sketch of the blueshifted jet/outflow system in AFGL 2591 emanating from the radio source VLA-3 and associated to the SE water maser cluster (Figure 2d-f). The inclination of the outflow axis about the line-of-sight ($\sim 30 - 45^\circ$) and on the plane of the sky ($\sim 10^\circ$) is reported. The NIR loops are shown as a cross section of the outflow projected along the plane of the sky. The water maser emission associated with VLA-3 emerges from the outflow walls and mainly expands toward the observer (Section 4.2).

Table 1. Radio continuum toward the VLA–3 component in AFLG 2591

Telescope	λ (cm)	HPBW mas \times mas at $^\circ$	Image rms (mJy beam $^{-1}$)	Peak position		F_{peak} (mJy beam $^{-1}$)	Deconvolution mas \times mas at $^\circ$
				Δx (mas)	Δy (mas)		
VLA–A	1.3	80×80	0.19	633 ± 10	-145 ± 10	1.24	88×38 at 88°
VLA–A	0.7	45×38 at -34°	0.11	633 ± 10	-145 ± 10	0.95	65 mas for slice at 75°
...	48 mas for slice at -48°
...	62 mas for slice at -159°

Note. — The 1.3 and 0.7 cm VLA–A measurements are from archival data (Trinidad et al. 2003; van der Tak & Menten 2005). The peak position in columns 5–6 is the relative position with respect to the reference feature of Table 2. Column 8 gives the deconvolved FWHM sizes of the Gaussian fits to the 1.3 cm emission and along the three axes of the 0.7 cm emission (position angles east of north).

Table 2. Parameters of VLBA 22.2 GHz water maser features.

Feature #	Detection (epochs)	V_{LSR} (km s ⁻¹)	F_{peak} (Jy beam ⁻¹)	Δx (mas)	Δy (mas)	V_x (km s ⁻¹)	V_y (km s ⁻¹)
North West Cluster							
1	1	-5.00	14.87	-39.72 ± 0.11	122.69 ± 0.05
2	1,2,3,4	-5.42	14.17	-78.51 ± 0.06	125.13 ± 0.05	4.0 ± 2.9	14.2 ± 2.3
3	1	-5.00	0.55	-46.13 ± 0.08	124.11 ± 0.05
Middle West Cluster							
4	1,2,3,4	-11.74	20.60	0 ± 0.06	0 ± 0.09
5	1,2,3,4	-5.42	13.41	-4.07 ± 0.12	4.16 ± 0.06	4.3 ± 3.2	14.6 ± 2.1
6	1,2,3,4	-6.68	8.29	0.02 ± 0.05	0.47 ± 0.07	6.9 ± 1.9	3.4 ± 2.2
7	1,2,3	-7.10	2.98	-12.47 ± 0.07	0.59 ± 0.06	-14.4 ± 3.3	-0.3 ± 4.1
8	1,2,3,4	-4.57	1.60	-3.91 ± 0.07	4.18 ± 0.07	8.5 ± 2.1	15.0 ± 2.2
9	1	-1.20	0.24	-0.37 ± 0.06	1.79 ± 0.08
10	4	-2.89	0.24	-16.96 ± 0.08	1.19 ± 0.12
11	1	-4.15	0.18	-11.78 ± 0.05	0.10 ± 0.06
12	1	-4.58	0.17	-3.04 ± 0.05	3.99 ± 0.06
13	4	-0.36	0.14	-14.65 ± 0.07	-0.97 ± 0.07
14	4	-6.26	0.09	-16.26 ± 0.07	1.51 ± 0.10
15	1	-7.94	0.09	-13.20 ± 0.06	1.38 ± 0.08
16	1	-1.20	0.06	-10.40 ± 0.07	-1.00 ± 0.06
North East Cluster							
17	1,2,3,4	-5.00	22.25	651.05 ± 0.06	305.69 ± 0.06	-2.5 ± 1.8	4.4 ± 2.1
18	1,2,3,4	-9.21	6.01	650.18 ± 0.05	317.22 ± 0.06	-7.5 ± 1.7	13.2 ± 2.0
19	1,2,3,4	-12.58	5.44	615.75 ± 0.06	295.33 ± 0.06	-7.5 ± 2.0	4.3 ± 2.5
20	1,2,3,4	-7.53	4.52	618.75 ± 0.10	208.02 ± 0.10	0.3 ± 2.2	-12.5 ± 2.4
21	1,2,3,4	-8.79	2.89	624.70 ± 0.06	312.39 ± 0.09	-13.2 ± 2.1	2.8 ± 2.1
22	1,2,3,4	-8.79	2.29	623.68 ± 0.11	312.34 ± 0.05	-5.5 ± 1.7	5.2 ± 2.0
23	4	-9.21	2.03	645.05 ± 0.06	316.82 ± 0.06
24	1,2,3	-8.37	2.01	655.31 ± 0.10	317.05 ± 0.07	11.3 ± 4.2	16.0 ± 4.3
25	2,3	-8.37	1.85	654.88 ± 0.08	317.44 ± 0.06
26	1,2,3,4	-7.53	1.60	608.52 ± 0.06	207.16 ± 0.06	-14.3 ± 1.8	-11.3 ± 2.2
27 ^a	1,2,3,4	-8.37	1.35	620.27 ± 0.19	311.32 ± 0.16
28	1,2,3,4	-7.11	0.69	625.15 ± 0.05	215.20 ± 0.05	8.5 ± 1.8	-1.7 ± 2.1
29 ^a	1,2,3	-6.69	0.53	625.44 ± 0.05	215.62 ± 0.06
30	1,2,3,4	-5.00	0.52	648.84 ± 0.08	306.30 ± 0.06	-4.0 ± 2.0	3.1 ± 2.0
31 ^a	1,2,3,4	-9.21	0.47	641.48 ± 0.09	315.73 ± 0.05
32	1,2,3,4	-8.27	0.42	631.55 ± 0.05	314.48 ± 0.06	-8.5 ± 1.8	5.4 ± 2.2
33	1,2,3,4	-9.63	0.40	625.42 ± 0.09	312.92 ± 0.10	-9.7 ± 2.1	6.4 ± 2.2
34	1,2,3	-8.37	0.39	653.85 ± 0.06	317.29 ± 0.24	14.1 ± 3.3	14.0 ± 8.7
35	1,2,3,4	-7.53	0.39	594.08 ± 0.05	223.24 ± 0.13	-14.4 ± 1.8	8.5 ± 2.2
36	2,3,4	-8.37	0.31	657.75 ± 0.06	309.98 ± 0.06	24.1 ± 3.0	5.7 ± 3.2
37	1,2,3	-6.26	0.24	658.35 ± 0.07	312.14 ± 0.09	18.0 ± 3.3	-11.0 ± 4.7
38	1,2,3,4	-6.69	0.23	688.86 ± 0.08	308.38 ± 0.14	1.4 ± 1.8	9.0 ± 2.2
39 ^a	1,2,3	-6.69	0.22	685.88 ± 0.05	311.26 ± 0.05
40	1,2,3,4	-6.69	0.19	626.85 ± 0.05	221.95 ± 0.06	5.8 ± 1.8	-0.2 ± 2.1
41	2,3,4	-7.53	0.19	620.88 ± 0.25	311.72 ± 0.08	-6.1 ± 3.7	0.5 ± 3.0

Table 2—Continued

Feature #	Detection (epochs)	V_{LSR} (km s ⁻¹)	F_{peak} (Jy beam ⁻¹)	Δx (mas)	Δy (mas)	V_x (km s ⁻¹)	V_y (km s ⁻¹)
R.A. (J2000)				Decl. (J2000)			
<u>20^h29^m24^s.8228</u>				40°11′19″.593			

Note. — For each identified feature belonging to a given cluster of maser emission, the label (given in Column 1) increases with decreasing brightness and the different epochs of detection are reported in Column 2. Columns 3 and 4 report the LSR velocity and brightness of the brightest spot of each feature, observed at the epoch underlined in Column 2. Columns 5 and 6 give the position offset at the first epoch of detection relative to the feature # 4 (centered on the phase-reference maser channel # 145) in the east and north directions, respectively. The uncertainties give the intensity-weighted standard deviation of the spots distribution within a feature and was combined in quadrature with a conservative 50 μ as uncertainty. This 50 μ as plateau accounts for deviations from a Gaussian fit assumption. The absolute position of the reference maser feature is reported at the bottom of the table and is accurate to within ± 1 mas. Columns 7 and 8 report the projected components of the feature proper motion relative to the feature # 4, along the east and north directions, respectively. A proper motion of 1 mas yr⁻¹ corresponds to 15.6 km s⁻¹ at a distance of 3.3 kpc.

^aFeatures with too uncertain proper motions (> 70%)